ADVANCED MATERIALS
www.advmat.de

Flexible and Self-Powered Photodetector Arrays Based on All-Inorganic $CsPbBr_3$ Quantum Dots

Kai Shen, Hao Xu, Xiao Li, Jian Guo, Sanjayan Sathasivam, Mingqing Wang, Aobo Ren, Kwang Leong Choy,* Ivan P. Parkin, Zhengxiao Guo, and Jiang Wu**

Flexible devices are garnering substantial interest owing to their potential for wearable and portable applications. Here, flexible and self-powered photodetector arrays based on all-inorganic perovskite quantum dots (QDs) are reported. CsBr/KBr-mediated $CsPbBr_3$ QDs possess improved surface morphology and crystallinity with reduced defect densities, in comparison with the pristine ones. Systematic material characterizations reveal enhanced carrier transport, photoluminescence efficiency, and carrier lifetime of the CsBr/KBr-mediated $CsPbBr_3$ QDs. Flexible photodetector arrays fabricated with an optimum CsBr/KBr treatment demonstrate a high open-circuit voltage of 1.3 V, responsivity of 10.1 A W^{-1}, specific detectivity of 9.35×10^{13} Jones, and on/off ratio up to $\approx 10^4$. Particularly, such performance is achieved under the self-powered operation mode. Furthermore, outstanding flexibility and electrical stability with negligible degradation after 1600 bending cycles (up to 60°) are demonstrated. More importantly, the flexible detector arrays exhibit uniform photoresponse distribution, which is of much significance for practical imaging systems, and thus promotes the practical deployment of perovskite products.

The "Internet of Things" (IoT) has been expected to reshape or even revolutionize human daily lives. As a fundamental technology of the IoT, flexible optoelectronics, such as solar power sources, display panels, and photodetectors, have attracted substantial research interest globally.[1–3] Moreover, high-performance photodetection is highly desirable in various fields, including optical communication, imaging, and environmental monitoring.[4–6] Currently, GaN, Si, InGaAs, and other semiconductors have dominated the ultraviolet to near-infrared photodetection market.[7–10] These detectors are mostly assembled on rigid substrates and usually require relatively thick active materials for photonic detection, therefore, they are not compatible with flexible systems or suitable for low cost manufacturing.

The demand for flexible devices has driven the research in emerging functional materials that are bendable. To date, various functional materials have been explored for constructing flexible photodetectors, such as zero-dimensional (0D) semiconductor nanostructures, 2D layered materials, and perovskites.[11–14] They can be facilely transferred to arbitrary rigid substrates and directly deposited on flexible substrates, which are favorable for flexible optoelectronics. Particularly, organometal halide perovskites (OHPs) have demonstrated intriguing properties, including large absorption coefficients, tunable bandgaps, long carrier diffusion length, and high carrier mobility.[15–20] Nevertheless, their organic parts

K. Shen, Dr. H. Xu, X. Li, Prof. J. Wu
Department of Electronic and Electrical Engineering
University College London
Torrington Place, London WC1E 7JE, UK
E-mail: hao.xu.15@uestc.edu.cn; jiangwu@uestc.edu.cn
Dr. H. Xu, Dr. A. Ren, Prof. J. Wu
Institute of Fundamental and Frontier Sciences
University of Electronic Science and Technology of China
Chengdu 610054, P. R. China
Dr. M. Wang, Prof. K. L. Choy
Institute for Materials Discovery
University College London
Torrington Place, London WC1E 7JE, UK
E-mail: k.choy@ucl.ac.uk
The ORCID identification number(s) for the author(s) of this article can be found under https://doi.org/10.1002/adma.202000004.
J. Guo, Dr. S. Sathasivam, Prof. I. P. Parkin
Department of Chemistry
University College London
20 Gordon Street, Bloomsbury, London WC1H 0AJ, UK
Prof. Z. Guo
Departments of Chemistry
The University of Hong Kong
Hong Kong, China
Prof. Z. Guo
HKU Zhejiang Institute of Research and Innovation
The University of Hong Kong
Hangzhou, China
Prof. Z. Guo
Department of Mechanical Engineering
The University of Hong Kong
Hong Kong, China

DOI: 10.1002/adma.202000004

have encountered air-exposure stability issues and are sensitive to ambient conditions, and seriously degrading the device performance. Noteworthy, low-dimensional all-inorganic cesium lead bromide quantum dots ($CsPbBr_3$ QDs) have been verified to exhibit better environmental stability.[21,22] Benefiting from the quantum confinement effect, $CsPbBr_3$ QDs show specific optical properties, such as tunable emission color by adjusting dot sizes and/or shape.[23] To overcome intrinsic shortcomings (such as high density of trap states and insulating barriers), the solutions for improving quantum yield and charge carrier balance of $CsPbBr_3$ QDs are essential and have been proposed, including the ligand density control, the atomic ligand scheme, and the ligand-exchange strategy.[24–26] As a result, high-temperature and/or complicated synthesis procedures were involved, yet conflicted with the philosophy of simple and cost-effective assembly for perovskites.

Here, a facile one-pot synthesis of all-inorganic $CsPbBr_3$ QDs is demonstrated at ambient conditions. Especially, the CsBr/KBr assisted strategy renders QDs with improved electrical and optical properties. As a result, flexible and self-powered photodetector arrays fabricated from the CsBr/KBr treated $CsPbBr_3$ QDs exhibit enhanced device performance. For instance, the responsivity and detectivity reach up to 10.1 A W^{-1} and 9.35×10^{13} Jones under self-powered operation, which is improved by over 300% and 1000%, respectively. In addition, the arrays exhibit noticeable folding endurance, electrical stability, and performance uniformity.

An effective and facile technique was developed to synthesize all-inorganic $CsPbBr_3$ QDs under ambient conditions,[18] as illustrated in the schematic flowchart in **Figure 1**a. First, the prepared Cs^+ and $PbBr_2$ precursors were mixed with hexane and 2-propanol, which immediately turned yellow within a few seconds. Subsequently, the CsBr/KBr precursor was injected into the mixture, with the fraction increased from 0.025 to 0.3. Here, this fraction was defined as $x = [Cs^+/K^+]/([Cs^+/K^+] + [Cs^+])$ in mols, representing $[Cs^+/K^+]$ in the CsBr/KBr precursor out of the total amount of monovalent cations in the solution. To avoid the interruption from other ligands, the CsBr/KBr precursor was prepared in the same solvent mixture as the $PbBr_2$ precursor. Centrifugation, purification, and re-dispersion were subsequently carried out to remove irrelevant solvents from the as-prepared colloidal $CsPbBr_3$ QDs. Spin coating and thermal annealing were then applied to induce film formation and enhance film quality.

The crystal structure of the as-synthesized colloidal $CsPbBr_3$ QDs was examined by transmission electron microscopy (TEM), as displayed in Figure 1b,c, and Figures S1–S3, Supporting Information. Both the pristine and the 0.025 Cs^+/K^+ assisted $CsPbBr_3$ QDs exhibit clear lattice fringes, with lattice constants of ≈2.91 and ≈2.72 Å, respectively (Figure S4, Supporting Information). This variation implied that the lattice compression can be associated with in-plane strains. By performing size distribution analysis (Figure S5, Supporting Information), it was determined that the average size of $CsPbBr_3$ QDs slightly decreased from 7.67 to 7.45 nm after blending CsBr/KBr additives, indicating smaller colloids. Energy dispersive X-ray spectroscopy (EDX) was subsequently implemented to examine the elemental distribution, as shown in Figure 1d. It is worth noting that there was a small amount of potassium (K) distributed uniformly in the film after introducing Cs^+/K^+, suggesting the successful incorporation of additives. In order to further verify the introduction of CsBr/KBr into the as-prepared perovskite films, X-ray photoelectron spectroscopy (XPS) analysis of the full spectra was performed, especially for the

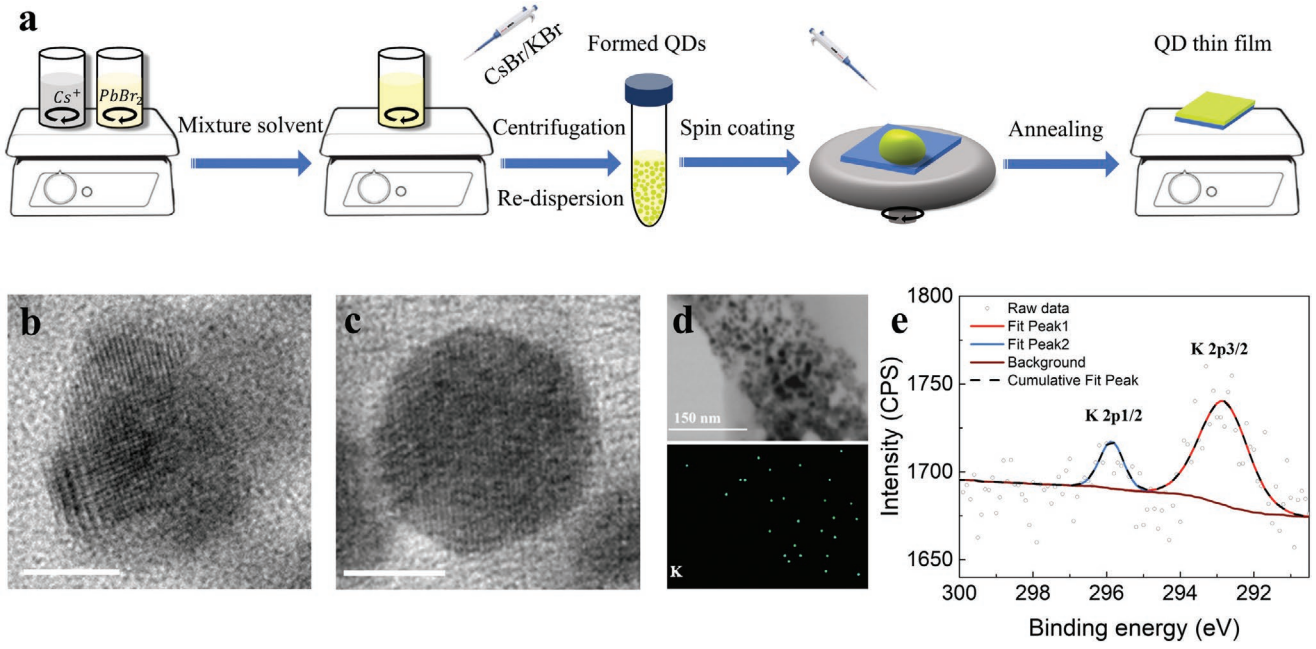

Figure 1. Synthesis at room-temperature and structural characterizations of CsBr/KBr assisted $CsPbBr_3$ QDs. a) A flowchart of the synthesis process of $CsPbBr_3$ QDs with CsBr/KBr treatment. b,c) TEM images of pristine $CsPbBr_3$ QDs (b) and 0.025 CsBr/KBr doped $CsPbBr_3$ QDs (c). The scale bars are 5 nm. d) Low-magnification TEM image and the corresponding elemental mapping (K). e) High-resolution XPS spectra of K 2p core level of CsBr/KBr assisted QDs thin film.

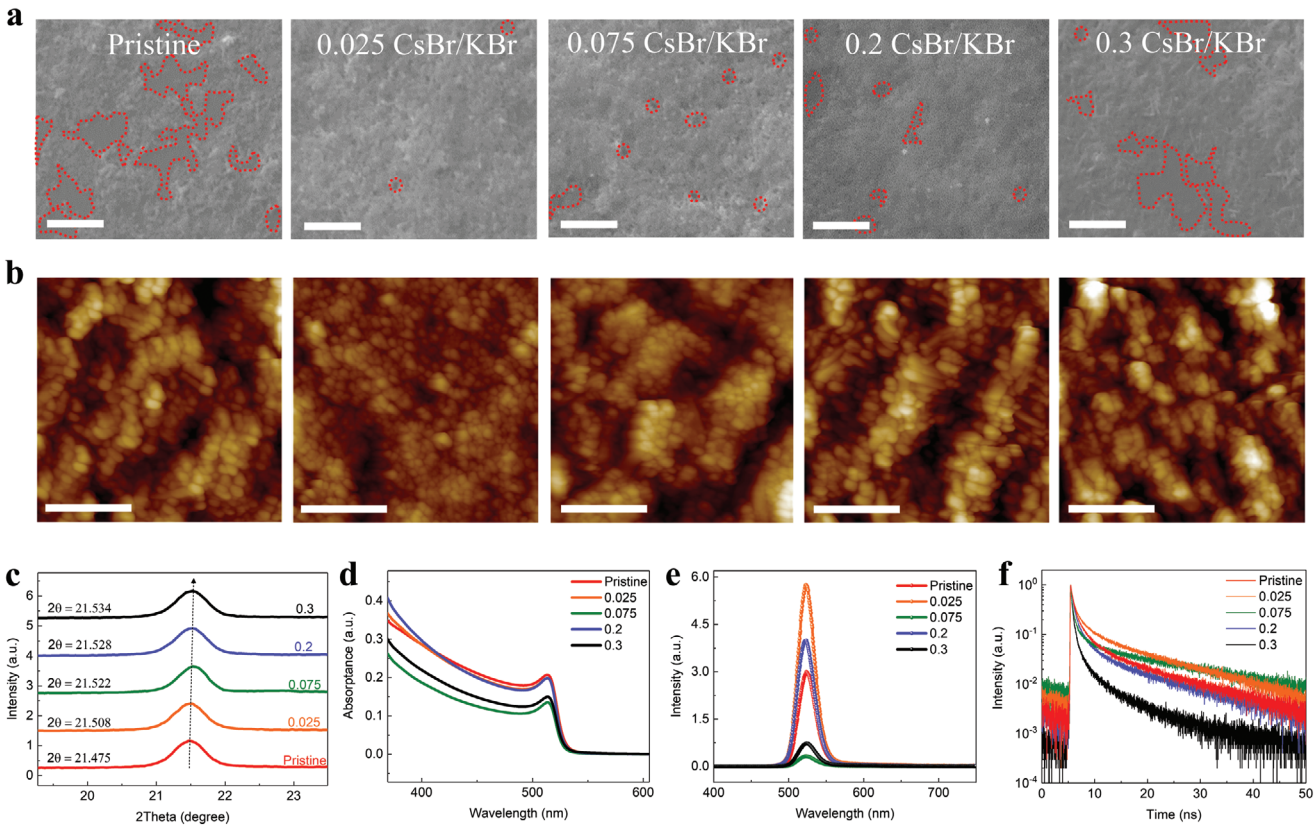

Figure 2. Evolutions of morphological characteristics and optical properties of the as-prepared QD film after different amount of CsBr/KBr treatments. a) The corresponding SEM images. Scale bar is 3 µm. b) AFM images obtained by the tapping mode, with the scale bar of 700 nm. The scanned dimension is 2 µm × 2 µm. c) The enlarged XRD measurement results. d) Absorption spectra of different QD films. e) Steady-state PL spectra and f) time-resolved PL decay curves excited by a 405 nm laser. Each color represents different injection ratios of CsBr/KBr.

core levels of Cs 3d, Pb 4f, Br 3d, and K 2p. Notably, the peaks (Cs 3d, Pb 4f, and Br 3d) all first shifted to higher binding energy when blending CsBr/KBr (x = 0.025), but to lower binding energy after introducing more additives (Figure S6, Supporting Information), implying the insertion of potassium cations induced impacts. According to the previous studies, the binding energies of lead cations and halides were not changed by slight perturbation of CsBr/KBr.[27,28] The increased binding energy, when a sufficient amount CsBr/KBr (x = 0.025) was added, revealed the enhanced interaction between Pb–Br and Cs–Br, which can reasonably lead to more stable crystal structures.[22,29–31] In Figure 1e, the two peaks located at 295.8 and 292.8 eV are evidently observed in the treated $CsPbBr_3$ QDs film rather than the pristine one, which were assigned to K 2p1/2 and K 2p3/2 states,[32] respectively (Figure S7, Supporting Information). This further confirmed the embedment of K^+ ions, in agreement with the EDX results.

The evolution of surface morphology with increasing x = 0.025–0.3 was evaluated by scanning electron microscopy (SEM), as displayed in **Figure 2**a. The large pinholes are clearly observed in the pristine perovskite film (marked as red dotted circles), indicative of a poor film coverage. In contrast, by introducing CsBr/KBr additives, the perovskite thin film exhibited more compact surface with much less and smaller pinholes, especially for the fraction of 0.025. Such improved surface coverage and film continuity of the 0.025 CsBr/KBr assisted perovskite thin film should stem from the distribution of smaller colloid as observed in TEM (Figure S5, Supporting Information),[33] and better substrate-philicity as identified by the smallest contact angle (Figure S8, Supporting Information).[34] Also, the morphological characteristics were further explored by atomic force microscopy (AFM) under the soft tapping mode at room temperature, as shown in Figure 2b. It is observed that small pinholes in the pristine film tended to reduce apparently after introducing CsBr/KBr (x = 0.025), but increase again when more additives were blended. Similar to the observation of pinholes, the overdosed additives aggravated the agglomerations of $CsPbBr_3$ QDs and thus led to a gradually roughened surface. Noteworthy, the CsBr/KBr (x = 0.025) mediated thin film exhibited a relatively smooth surface with the smallest surface roughness of ≈17.6 nm (Table S1, Supporting Information), which can be resulted from the suppressed agglomerations. This significant improvement for surface morphology revealed the effective additive treatment for $CsPbBr_3$ QDs, which can potentially facilitate the carrier transport and reduce leakage current.

In addition, X-ray diffraction (XRD) measurements were performed to explore crystal lattice features of the $CsPbBr_3$ QDs. As displayed in Figure S9, Supporting Information, there is no additional peaks resolved as the additive was injected, revealing the introduction of CsBr/KBr did not interrupt the original crystallinity. However, as shown in Figure 2c, the Eigenpeak

located at 21.8°, corresponding to the (112) plane of the orthorhombic $CsPbBr_3$ structure,[18] is slightly shifted to the right due to the interplanar spacing transition. This indicates a declined *d*-spacing along with the additive injection according to the Bragg's equation ($2d\sin\theta = n\lambda$), in a good agreement with the TEM results.[35]

To gain a further insight into the influences of additive on perovskite films, optical properties were systematically characterized using UV–vis spectroscopy, PL, and time-resolved PL (TRPL). As shown in Figure 2d, the steady-state absorption spectra of the doped $CsPbBr_3$ QDs films exhibit sharp absorption edges at around 530 nm. In order to determine the corresponding optical bandgap energy (E_g), all the spectra were plotted with the Tauc method (Figure S10, Supporting Information). It is worth noting that CsBr/KBr doping introduced a slight blueshift from 2.340 to 2.348 eV due to the aforementioned compressed lattice and reduced colloid size,[36] implying the incorporation of CsBr/KBr mixtures induced influence. Figure 2e exhibits the emission features of QD films under a 405 nm laser excitation. As clearly resolved, all the peaks remained symmetric and sharp after the introduction of additives. By comparing the peak positions, they are slightly blueshifted from 524.5 to 522 nm as the additives were implanted (Figure S11a, Supporting Information), showing a similar tendency to the UV–vis results. Notably, the $CsPbBr_3$ QDs film with proper CsBr/KBr addition (x = 0.025) exhibits the narrowest FWHM ≈ 26 nm (Figure S11b and Table S2, Supporting Information), indicating the improved emission and crystal quality. These features suggested relatively efficient emission attributed to the agglomeration suppression, and are promising for the light-emitting applications.

Furthermore, the normalized TRPL decay plots in Figure 2f were obtained to study the carrier dynamics after the doping processes. They were fitted by a bi-exponential function with two decay components, as shown in Figure S12, Supporting Information. Accordingly, the time constants of τ_1 and τ_2, and the corresponding fractions of f_1 and f_2 are summarized in Table S3, Supporting Information, in which the average lifetimes of the $CsPbBr_3$ QDs with different doping levels were calculated as 4.95, 7.53, 7.95, 4.24, and 1.81 ns, respectively. As listed, the carrier lifetimes were prolonged over 50% for CsBr/KBr assisted perovskite films when the blending fraction was x = 0.025 and 0.075. This can be attributed to the intermediate energy levels induced by the interstitial cations and deep trap states, as explored in the previous report.[37] However, the carrier lifetimes reduced with further introduction of CsBr/KBr (x > 0.075), which was likely due to the presence of more impurities that introduced non-radiative recombination centers after excessive treatment. Physically, these centers can provide local sites for fast relaxation of photoexcited excitons. Accordingly, it was reasonable to assume that the enhanced PL lifetime should originate from the effective suppression of exciton recombination in the QD films, indicating the improved crystal quality after appropriate CsBr/KBr blending. To sum up, the introduction of CsBr/KBr additives helped to form dense and uniform surfaces with less defects, as well as retaining high crystallinity. The systematic characterizations validated that the 0.025 CsBr/KBr doped $CsPbBr_3$ QDs exhibited relatively more suitable features for optoelectronics. For instance, 0.025 Cs^+/K^+ assisted $CsPbBr_3$ QDs exhibited superior light emission and absorption capability, which were expected to be desirable candidates for flexible photodetectors.

To further identify the CsBr/KBr treatment induced effects, all-inorganic $CsPbBr_3$-QD-based flexible photodetector arrays were fabricated from perovskite films with the CsBr/KBr addition fraction "x" varied from 0.025 to 0.3. As shown in **Figure 3a**, the as-fabricated photodetector arrays possessed good flexibility. Figure 3b,c shows the optical images of the flexible photodetector array placed on a purpose-designed stage without and with illumination, respectively. As clearly displayed, there are nine sections allocated for every chip, where each section is comprised of 8 × 11 pixels to form photodetector arrays. All devices share the same bottom electrode (ITO), and each pixel possesses an individual top contact (Ni/Au). The detailed dimension of each pixel is listed in Figure S13, Supporting Information.

Subsequently, photoresponsive characteristics of these photodetectors were measured under illumination of 405, 450, and 520 nm lasers at room temperature, respectively. Figure 3d shows the typical logarithmic current–voltage (*I*–*V*) curves of the CsBr/KBr treated photodetectors (x = 0.025), which exhibits evident photoresponse owing to the direct bandgap transition. Also, a similar phenomenon was observed for other treated devices (Figure S14, Supporting Information). It is worth noting that the 0.025 doped photodetector not only exhibited low dark current (0.1 μA) but also a large open-circuit voltage (V_{oc}) up to 1.3 V, as discussed below.

According to the *I*–*V* curves in Figure 3e, the CsBr/KBr treated photodetectors exhibited the largest photoresponse current (I_{light} = 223 μA), reverse biased at –1.5 V and illuminated by the 405 nm laser, when the blending fraction x = 0.025. This photocurrent was ≈91% larger than the control device. Similar behavior was also observed for the 450 and 520 nm laser excitation (Figure S15, Supporting Information), indicating more efficient electron–hole generation and collection for the 0.025 CsBr/KBr treated photodetectors. Meanwhile, a smaller dark current was achieved for the photodetector arrays based on both 0.025 and 0.075 CsBr/KBr doped $CsPbBr_3$ QDs, almost tenfold lower than the pristine device (Figure 3f). This improvement was consistent with the morphology evolution characteristics (Figure 2a,b), which suggests the importance of adding a proper fraction of CsBr/KBr. Additionally, the V_{oc} of each device under different illuminations were evaluated from the corresponding *I*–*V* curves, as shown in Figure 3g. Obviously, the V_{oc} reached the highest value (1.22, 1.30, and 1.30 V) for the three different wavelengths when the fraction was 0.025, suggesting a strong induced photovoltaic effect. Moreover, the corresponding ratio of I_{light} and dark current (I_d) was significantly enhanced for the 0.025 CsBr/KBr doped photodetector under different laser sources, especially operating at the self-powered mode (Figure S16, Supporting Information). For instance, it reached up to 3.6×10^6 under 405 nm laser illumination, two orders of magnitude larger than the controlled device, which was even comparable with the commercial photodetectors.

Responsivity (R_A) and specific detectivity (D^*), as the typical figure-of-merits, identify the capability of a photodetector responding to a light source, and the weakest level of light that can be detected, respectively.[38] R_A is expressed by $R_A = I_{ph}/P$,

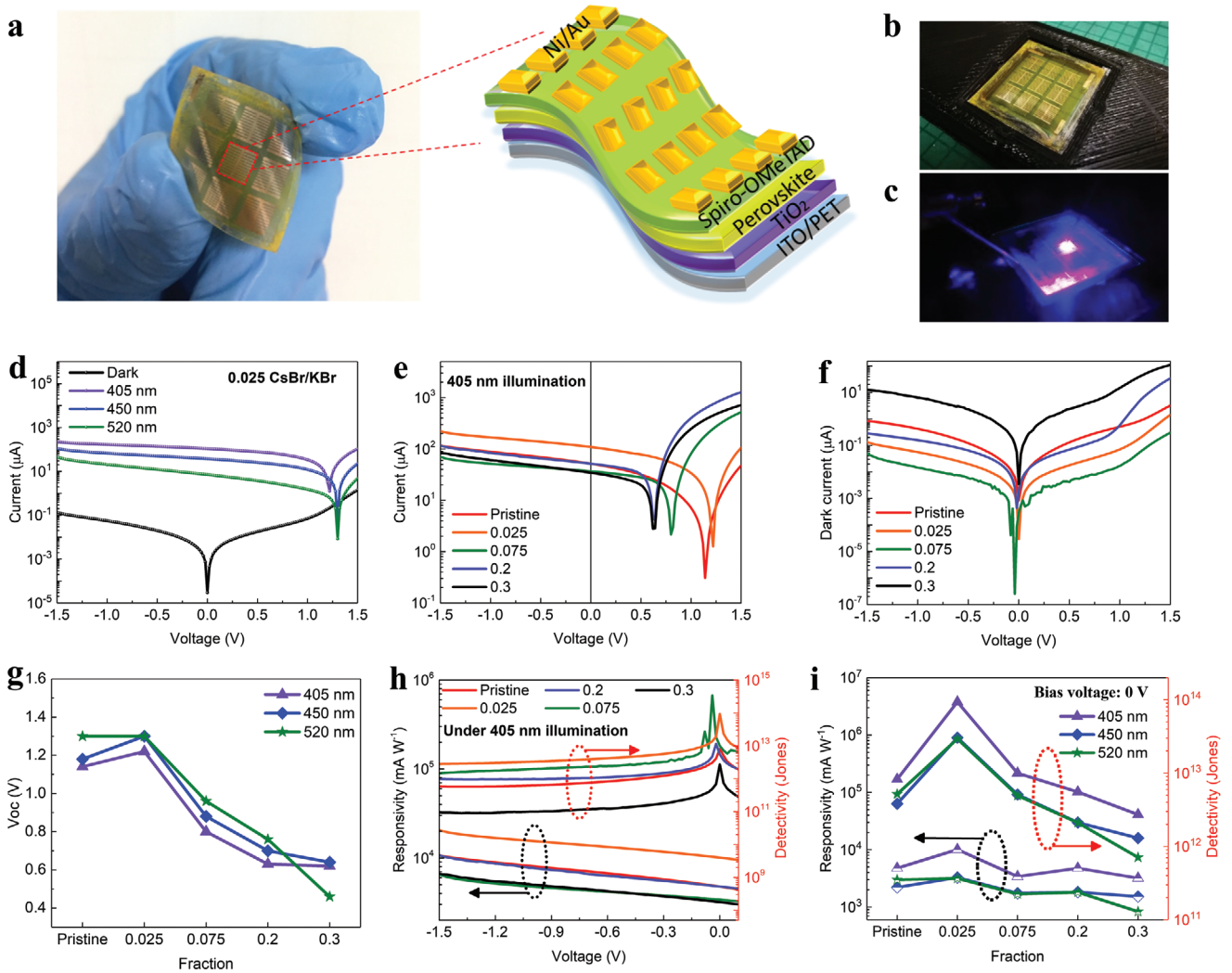

Figure 3. Photoresponse characteristics of the $CsPbBr_3$-QD-based flexible photodetector arrays with CsBr/KBr treatment, with $x = 0$, 0.025, 0.075, 0.2, and 0.3. a) Digital images of flexible photodetector arrays (left), and the schematic representation of device architecture in a single section (right). b,c) Digital photographs of the flexible photodetector arrays placed on the purpose-designed sample holder without (b) and with (c) the laser illumination. d) Typical logarithm *I–V* curves of the 0.025 CsBr/KBr doped single device in dark, and under 405, 450, and 520 nm laser illumination. e) Light current comparison. f) Dark current comparison. g) Open-circuit voltage variation, with different light excitations. h) Responsivity and detectivity of five devices with different CsBr/KBr treatments, as a function of applied bias, excited by 405 nm laser diode with a power intensity of 13.4 mW cm^{-2}. i) The corresponding wavelength-dependent responsivity and detectivity, measured at zero bias voltage.

where I_{ph} represents photocurrent ($I_{ph} = I_{light} - I_{dark}$), and P denotes the incident light power). Assuming that shot noise from the dark current is the major contributor to the total noise, D^* can be defined as $D^* = R_A/(2qJ_d)^{1/2}$, where J_d is the dark current density. Consequently, all the devices exhibit good R_A (>3.2 A W^{-1}) and D^* (>1 × 10^{11} Jones), as shown in Figure 3h. Noteworthily, the best R_A and D^* were achieved from 0.025 CsBr/KBr assisted device, as large as 21 A W^{-1} (at –1.5 V bias) and 9.35 × 10^{13} Jones (at 0 V bias) under 405 nm laser illumination, respectively. This phenomenon was further validated by the 450 and 520 nm radiation (Figure S17, Supporting Information). Furthermore, the corresponding R_A and D^* variation tendencies at the specific bias voltages were extracted in Figure S18, Supporting Information. Evidently, the performance of the 0.025 CsBr/KBr doped device maintained a dominant state under different laser illumination, consistent with the improved film properties. The figures-of-merit of photodetectors operating under the self-powered mode are plotted in Figure 3i. Similarly, the 0.025 CsBr/KBr assisted photodetectors triumphed under different light illumination. Namely, R_A and D^* were both significantly improved after the 0.025 CsBr/KBr treatment, reaching up to the maxima that were more than twofold and tenfold larger than the untreated device, respectively. Overall, the best pixel exhibited a responsivity of 21 A W^{-1} (at a bias of –1.5 V), high detectivity with 9.35 × 10^{13} Jones (self-powered mode), large open-circuit voltage of 1.30 V, and large external quantum efficiency (EQE) over 6400%. Such exciting photoresponse performance can be attributed to the combination of improved film formation, enhanced crystal quality, and efficient carrier generation, extraction, and transportation.

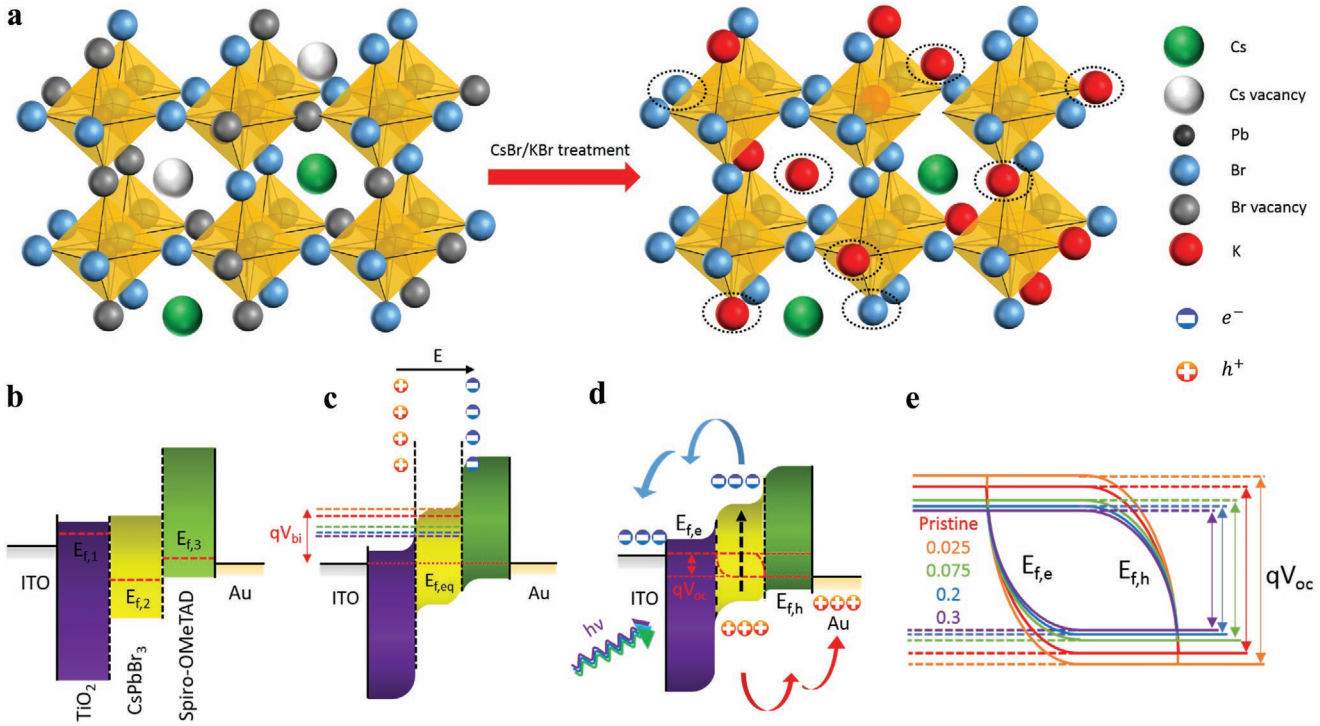

Figure 4. Mechanisms of additive-assisted strategy. a) Schematic crystal structures of the $CsPbBr_3$ QDs with CsBr/KBr meditation. b–d) Simplified energy band diagrams of the as-fabricated photodetectors: b) before contact; c) contact until reaching thermal equilibrium; d) under illumination (self-powered mode). e) The corresponding V_{oc} distribution. Upper and lower lines represent $E_{f,e}$ and $E_{f,h}$, respectively.

These results further confirm the benefit of introducing appropriate CsBr/KBr additives, which is favorable for constructing high-performance optoelectronics.

To understand the mechanisms behind the CsBr/KBr treatment scheme, schematic crystal structures were constructed, as displayed in **Figure 4**a. During the synthesis process, the involved ligands and/or solvent molecules can compete with halide ions to form distorted octahedral, where carrier excitation and recombination processes occurred.[39,40] This resulted in a large number of Br^- vacancies, which cannot be fully compensated due to the fast nucleation rate.[41] These Br^- vacancies were likely to introduce trap states in energy band structures, which affected carrier recombination dynamics and thereby degraded optical properties and device performance. Accordingly, the CsBr/KBr doping scheme first introduced excess Br into the perovskite precursor solutions to create a Br-rich environment and fill partial vacancies, favorable for the growth of high-quality $CsPbBr_3$ QDs.[42] Second, as demonstrated in previous literatures, excess K^+ can enter the interstitial or substitial sites of the perovskite lattice due to the smaller radius (0.138 nm) compared with Cs^+ (0.167 nm), and further compensated halide vacancies to reduce the defects.[43,44] Thereby, it was reasonable to deduce that both nonradiative recombination and halide migration can be inhibited in the CsBr/KBr mediated perovskite film, inducing an enhanced PL intensity and prolonged carrier lifetime. This is well supported by the PL and TRPL measurements (Figure 2e,f). In addition, K^+ with smaller ionic radius was able to partially fill A-site vacancies (Cs^+) by occupying the cavity of the Pb–Br framework, resulting in a compressed lattice constant and slight blueshift. Consequently, the additional Cs^+ can sufficiently react with the excess $PbBr_2$ to achieve higher yield and to avoid forming $CsPbBr_3$ derivatives, such as $CsPb_2Br_5$.[18,45] Based on the comprehensive material characterizations, the optimal CsBr/KBr content can be determined as 0.025. This doping level can balance properties of crystallinity, surface morphology, and radiative efficiency, which were thereupon expected to exhibit relatively better performance.

Subsequently, the schematic band structures are illustrated in Figure 4b–e, and the corresponding mechanisms for photodetector operation were explored below. Before contact, the Fermi energy levels (E_f) of each material are discrete and highlighted as red dashed lines, e.g., TiO_2 ($E_{f,1}$), $CsPbBr_3$ ($E_{f,2}$), and spiro-OMeTAD ($E_{f,3}$), regarding to the vacuum level (Figure 4b). As each layer contacted in dark, E_f are aligned across any interfaces until reaching the thermal equilibrium, as illustrated in Figure 4c. Noteworthy, the built-in potential V_{bi} is essential to be identified for deeply exploring the influence of additives in the perovskite layer, owing to its strong impact on charge separation and collection, and the maximum V_{oc}.[46–48] In this case, the built-in potential (V_{bi}), induced by E_f offset, was equivalent to largest E_f difference within the device, namely, between $E_{f,1}$ and $E_{f,2}$.[47] By performing ultraviolet photoelectron spectroscopy (UPS), $E_{f,2}$ of the CsBr/KBr assisted perovskite layers were determined to be ≈5.54, 5.71, 5.18, 5.13, and 5.06 eV, with increasing the fraction from 0 to 0.3, respectively (Figure S19, Supporting Information). By taking account of the reported value of $E_{f,1}$,[49] the theoretical V_{bi} were calculated as 1.23, 1.40, 0.88, 0.82, and 0.75 eV, respectively. The modulated E_f by using the additive-assisted strategy results in the largest V_{bi} from 0.025 CsBr/KBr treated devices, suggesting more efficient charge separation,

transportation, and collection. As the photodetector is under appropriate illumination (Figure 4d), the incident photons generate electron–hole pairs due to the intrinsic absorbing property of the perovskite active layer. Thanks to the strong V_{bi}, electron–hole pairs are efficiently separated. The resulted electrons and holes transport in the opposite direction, from $CsPbBr_3$ to TiO_2 and from $CsPbBr_3$ to spiro-OMeTAD, and finally collected by ITO and Ni/Au, respectively. It is logical to believe that an enhancement of carrier collection yield larger photocurrent in the 0.025 additive assisted photodetector owing to the aforementioned strongest V_{bi}, as validated by the *I–V* results in Figure 3e. Noteworthy, the carrier movement further induced the splitting of $E_{f,eq}$ into the electron quasi-fermi level ($E_{f,e}$) and the hole quasi-fermi level ($E_{f,h}$) at the cathode and anode, respectively, resulting in the formation of V_{oc}. Consequently, as the origin of self-powered operation, the corresponding V_{oc} distribution can be reasonably deduced based on the theoretical calculations. As resolved in Figure 4e, the V_{oc} trend is consistent with *I–V* results (Figure 3e,g). It is worth noting that the excess CsBr/KBr additives treatment leads to the smaller E_f and introduces more impurities within the perovskite layer, resulting in a V_{oc} loss due to the nonradiative recombination. On the contrary, this loss in V_{oc} is effectively inhibited in the treated perovskite film with the optimum fraction of 0.025, e.g., verified by the prolonged carrier lifetime in Figure 2f. These explorations further explained the corresponding results of device performance and provided the clear understanding of device mechanisms.

As aforementioned, the 0.025 CsBr/KBr doped $CsPbBr_3$ QDs demonstrated more advantages over the pristine and other doping levels, including superior R_A, D^*, and large V_{oc}, thus further investigations were carried out for the photodetectors enabled by them to obtain a comprehensive knowledge of their performance. In **Figure 5**a, the power-dependent *I–V* characteristics were obtained under the 405 nm laser illumination with the varied power intensities. As the incident power gradually increased, the increment of photoresponse current was accordingly observed, attributed to the increased photoexcited electron–hole pairs. The similar tendency is also observed under 450 nm and 520 nm laser illumination (Figure S20, Supporting Information). In Figure 5b, the power-dependent photocurrent obtained at the self-powered mode can be fitted by the power law ($I_{ph} \sim P^{\beta}$), where β is the exponent. β was determined as ≈1.076 and ≈0.805 for 405 and 450 nm laser illumination, respectively, indicating a low recombination rate. This relationship was also observed for the biased devices (Figure S21, Supporting Information). Interestingly, Figure S21d, Supporting Information, shows that the non-unity exponent became closer to a linear one as the applied voltage reduced. Additionally, Figure 5c shows the time-resolved photoresponse at different bias voltages, illustrating the good photo-switching characteristics. The current rose/fell immediately when the laser was turned on/off, and the saturated level enlarged with the bias voltage, due to the stronger external electrical field to separate electron–hole pairs more efficiently. A similar phenomenon was also observed for the 450 nm laser excitation (Figure S22, Supporting Information). In addition, the transient photoresponse excited by different wavelength lasers without external bias was examined, as shown in Figure 5d. Sensitive and reproducible cycles with a large on/off ratio of ≈2.1×10^4 was achieved, along with distinctive wavelength selectivity. The same phenomenon is also found with other applied bias voltage (Figure S23, Supporting Information). In comparison with the pristine devices in the self-powered mode, not only ≈40% higher photo-induced current was achieved for the 0.025 CsBr/KBr treated device, but also ≈248% shorten response time (Figure S24, Supporting Information), indicative of much more efficient charge extraction. This further revealed the benefits of the additive optimization scheme for improving photoresponse features.

Apart from the impressive performance, 0.025 CsBr/KBr mediated photodetector also exhibited evident flexibility and reproducibility, as investigated below. Figure 5e illustrates the transient output photoresponse features of the device at 0° and 60°, respectively, under different laser illumination. No obvious change of dark current in the flexible photodetector was identified before and after bending. In terms of the photo-induced current, it retained ≈94% of original value after 60° bending. Furthermore, the time-dependent photoresponse was examined after different bending cycles from 0 to 1600, when the photodetector was at self-powered mode (Figure 5f). It is observed that both dark current and photoresponse current maintain ≈93% of the original values even after the 1600 bending cycles, indicating strong folding endurance and electrical stability. Moreover, the mediated photodetectors exhibited excellent long-term stability with marginal degradation of photoresponse dynamics, after being stored under ambient conditions for over 7 months (Figure S25, Supporting Information).

Lastly, the uniformity of device performance, in terms of R_A, D^*, and V_{oc}, of the flexible photodetector arrays was determined below. The optical image of an individual section is displayed in Figure 5g, which consists of 8×11 pixels as indicated by the dashed lines. The 0.025 CsBr/KBr assisted devices were characterized under the self-driven mode, excited by a 405 nm light source with a power intensity of 13.4 mW cm^{-2}. Figure 5h–j shows the spatial distributions of the R_A, D^*, and V_{oc} of each pixel, corresponding to the pixels in Figure 5g. Thereupon, high performance is demonstrated in the self-driven photodetector arrays. In comparison with other perovskite-based photodetectors, our devices deliver competitive or even superior performance, as summarized in **Table 1**.[50–58] According to the map color variation, over 80% devices exhibited similar performance, indicating spatial photoresponse uniformity.

In summary, the $CsPbBr_3$ QDs with improved properties were successfully synthesized via the CsBr/KBr treatment under ambient conditions. Specifically, a small amount ($x = 0.025$) of CsBr/KBr injection evidently improved the surface morphology, beneficial for better carrier transport and lower leakage current. Additionally, the optimized perovskite QDs not only exhibited good crystallinity but also enhanced optical properties. Thanks to the optimized $CsPbBr_3$ QDs, flexible photodetector arrays exhibited a high responsivity of 10.1 A W^{-1}, detectivity approaching 10^{14} Jones, and a large on/off ratio over 10^4, under self-powered operation mode. Meanwhile, the device possessed noticeable stability and flexibility after 1600 bending cycles. More importantly, the as-fabricated photodetector arrays exhibited good uniformity in terms of device performance and *I–V* characteristics of each pixel. The self-powered and flexible

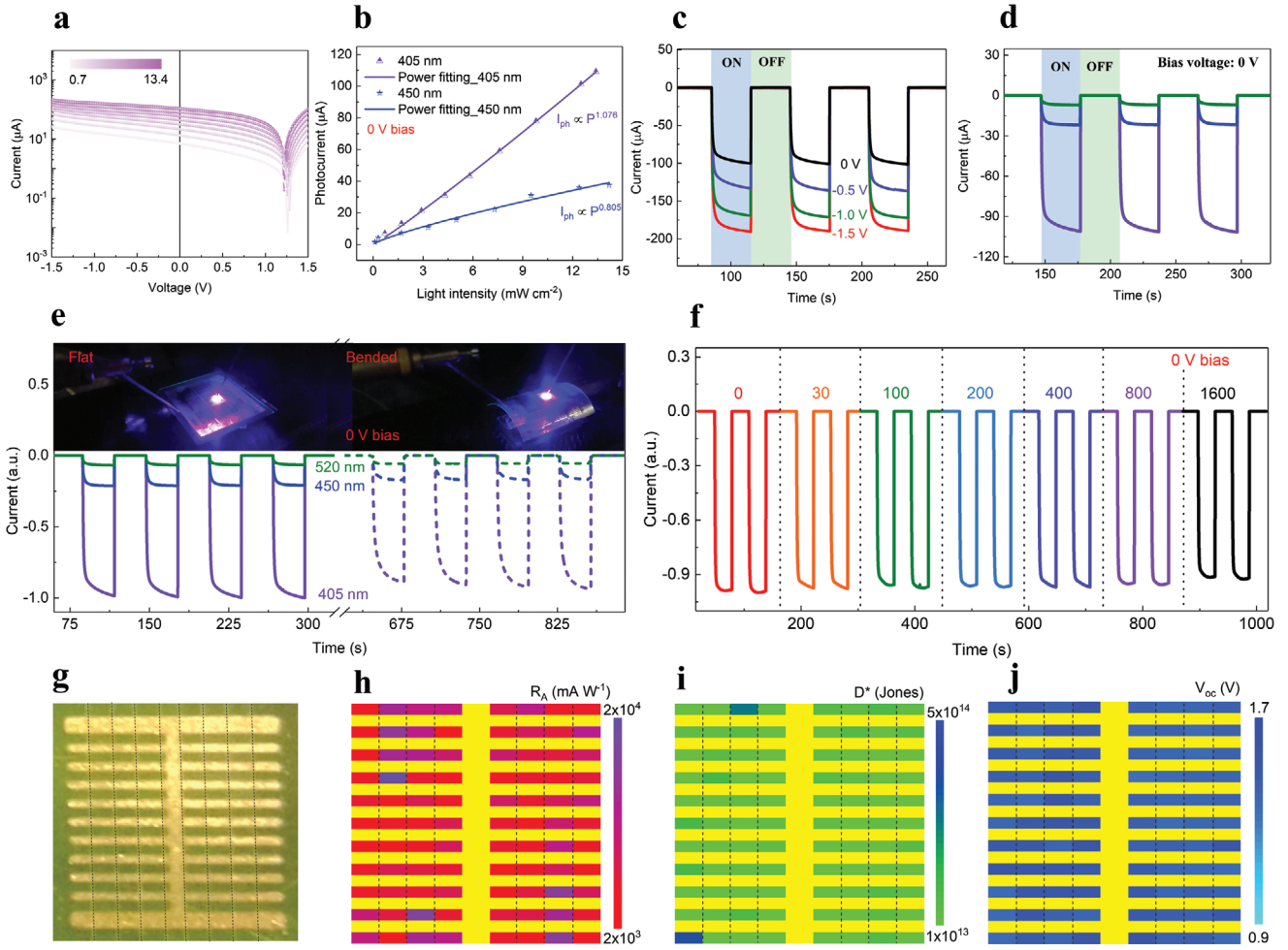

Figure 5. Photoresponse characteristics and electrical stability of the 0.025 CsBr/KBr doped flexible photodetector arrays. a) Typical logarithmic *I–V* characteristics under the 405 nm laser illumination, with the power intensity varying from 0.7 to 13.4 mW cm^{-2}. b) The corresponding photocurrent as a function of the incident intensity using the 405 and 450 nm light sources, and fitted by a power law. c) Transient photoresponse when the device was applied with different bias voltages. The 405 nm laser diode with a power intensity of 13.4 mW cm^{-2} was employed as the illumination source and generated periodical laser pulses. d) Wavelength-dependent temporal response under the self-power operation. e) The normalized transient photoresponse with different bending angles, 0° (solid lines) and 60° (dashed lines), under 405, 450, and 520 nm illumination at a fixed intensity of 13.4, 14.2, and 3.3 mW cm^{-2}, respectively. The insets are the corresponding photographs of the device when tested. f) Time-dependent on/off switching behavior of flexible photodetector arrays before and after 30, 100, 200, 400, 800, and 1600 bending cycles, illuminated by 405 nm laser diode with 13.2 mW cm^{-2}. g) The optical image of 8 × 11 pixelated flexible photodetector arrays in a single section. h–j) The spatial distribution of responsivity, detectivity, and open-circuit voltage mapping for a single section, respectively.

Table 1. Performance comparisons of reported perovskite photodetectors.

Active Materials	*R* under self-power [A W^{-1}]	*R* under bias [A W^{-1}]	*D** (Jones)	On/off	Reference
$CsPbBr_3$:ZnO	0.0115	0.0112 (0.1 V)	–	12.86	[50]
$CsPbBr_3$ microcrystals	–	6 (3 V)	≈10^{13}	<10	[51]
$CsPbBr_3$ nanosheets/CNTs	–	31.1 (10 V)	–	90	[52]
$CsPbBr_3$ single crystals	0.028	–	1.7×10^{11} (0 V)	10^5	[53]
$CsPbCl_3$ nanocrystals	–	1.89 (5 V)	–	10^3	[54]
$MAPbI_3$/CdS10	0.48	–	2.1×10^{13} (0 V)	750	[55]
$MAPbI_3$	–	0.1 (10 V)	1.02×10^{12}	300	[56]
$MAPbI_{3-x}Cl_x$	–	2.17 (5 V)	9.4×10^{11}	1.2×10^3	[57]
$MAPbI_3$/Spiro	21.5	–	3×10^{12} (0 V)	79.1	[58]
$CsPbBr_3$ QDs	10.1	21.2 (–1.5 V)	9.35×10^{13} (0 V)	2.1×10^4	This work

photodetector arrays with high performance are promising for portal optoelectronics.

Experimental Section

Materials: Cesium carbonate (Cs_2CO_3, 99%), lead(II) bromide ($PbBr_2$, 99.9%), cesium bromide (CsBr, 99.9%), titanium dioxide (TiO_2, 99.5%), 2,2′,7,7′-tetrakis(*N*,*N*-di-*p*-methoxyphenylamine)-9,9-spirobifluorene (spiro-OMeTAD, 99%), butylamine (99.5%), 2-propanol (99.5%), propionic acid (99.5%), hexane (99.5%), toluene (99.8%), 4-tert-butylpyridine (98%), lithium bis(trifluoromethylsulphonyl)imide (99%), chlorobenzene (99.8%), and indium tin oxide (ITO) coated polyethylene terephthalate (PET) (130nm, 60 Ω sq^{-1}) were purchased from Sigma–Aldrich. Potassium bromide (KBr, 99%) was purchased from Fisher Chemical. All solvents were anhydrous, and chemicals were used as received without further purification.

Synthesis: Cs^+- and $PbBr_2$-based precursors were first prepared by dissolving 3.6 mmol Cs_2CO_3 powders into 2 mL propionic acid, and loading 2.5 mmol $PbBr_2$ powders in a 5 mL mixed solvents of butylamine, 2-propanol, and propionic acid (1:1:1), respectively. Meanwhile, CsBr (22.6 µmol) and KBr (67.1 µmol) powders were dissolved in the mixture solvents (2 mL), the same as $PbBr_2$ precursor, to form CsBr/KBr precursor. To a solution of Cs^+ precursor (12.5 µL), 2-propanol (2.5 mL), and hexane (5 mL), $PbBr_2$ precursor (135 µL) was swiftly injected under continuous stirring. This solution turned light yellow turbid within seconds followed by immediate injection of CsBr/KBr precursor from a fraction of 0.025 to 0.3. The actual incorporation percentages of potassium in $CsPbBr_3$ QDs synthesized with different CsBr/KBr fractions in each sample were estimated as 0.37, 1.13, 3.03, and 4.31 at.%, respectively, by XPS. The high-quality $CsPbBr_3$ QDs were then obtained by centrifugation and purification to eliminate the trace of other solvents, and finally re-dispersed in toluene. Different centrifuge speeds of 1500 and 2000 rpm were applied for 2 min each time. All procedures were carried out at room temperature under ambient conditions.

Material Characterization: Additive-assisted samples on Cu grid were subjected to TEM measurements and EDX mapping using a JEOL 2100 microscope upon a Cu grid, attached with an X-Max^N detector (Oxford Instruments). XPS measurements were recorded using a Thermo Scientific K-alpha photoelectron spectrometer with monochromatic $Al_{k\alpha}$ radiation, and analyzed with CasaXPS. The morphological analyses of the samples were examined by conducting scanning electron microscopy (EVO LS15, ZEISS), and atomic force microscopy (Bruker Dimension Icon with ScanAsyst) with a soft tapping mode in the air. Additionally, contact angles were measured using Theta optical tensiometer (Attension), and XRD patterns were obtained by the PANalytical X'Pert PRO X-ray diffractometer with a Cu $K_{\alpha 1,2}$ excitation (λ = 1.540598 Å). Absorption spectra were recorded by Lambda 750S UV–vis spectrometers (Perkin Elmer) at room temperature, with a wavelength range of 250 to 800 nm. Steady-state and time-resolved PL spectra were measured by TCSPC (LifeSpec-ps, Edinburgh Instruments), equipped with a 405 nm laser diode at –16 °C, and fitted with bi-exponential decay function on fluorescence analysis software technology (FAST). UPS measurements were performed on a Thermo theta probe spectrometer with a base pressure of 5×10^{-10} mbar using He (I) UV light with photon energy of 21.22 eV. Photoelectron kinetic energy was measured using a hemispherical analyzer with angular acceptance over a solid angle of 60°.

Device Fabrication: The ITO-coated PET substrates were employed as the conductive flexible substrates, and were cleaned in the sequence of detergent, deionized water, and acetone with ultrasonication for 15 min, followed by plasma treatment (UV ozone) for 5 min. A highly uniform TiO_2 layer was subsequently deposited onto the flexible substrate by atomic layer deposition (Ultratech, Savannah G2 S200) at 100 °C, with 100 cycles to prevent the damage from the high temperature. Subsequently, a QD absorption layer was formed by spin coating the as-synthesized $CsPbBr_3$ QD solution with different CsBr/KBr treatments at 1000 rpm for 60 s. Several deposition cycles were applied to increase the absorption layer thickness, followed by annealing at 120 °C for 1 min after each spinning, and baking at 120 °C for 5 min after the last layer coating. It should be noted that annealing process plays an important role in the QD film quality or hence the device performance. One should bear in mind that further optimization of the annealing conditions may potentially lead to further improvement in device performance.[59,60] Subsequently, spiro-OMeTAD, as hole-transporting layer, was spin coated at 2000 rpm for 30 s, and dried in the air for 12 h.[13] The Ni/Au (10/100 nm) electrodes were finally deposited through a shadow mask by thermal evaporation under high vacuum (1×10^{-7} Pa), and were sliced using Karl Suss Scriber (RA120) to form arrays with dimension 153 µm × 526 µm of an individual pixel.

Device Measurements: Electrical measurements of devices were performed using a Keithley 4200 semiconductor characterization system, attached with an anti-vibrated probe station and a purpose-designed sample stage. Three laser diodes (wavelengths of 405, 450, and 520 nm) were employed as the illumination source and shined from the back of devices. Their corresponding power intensities were measured as 13.4, 14.2, and 3.3 mW cm^{-2}, respectively, by a LOT solar simulator system. The typical *I*–*V* curves were measured with voltage-sweeping mode from –1.5 V to 1.5 V, where the corresponding R_A and D^* were extracted from. The corresponding EQE was calculated as $EQE = R_A \times h \times c/(e\lambda)$, where h denotes Planck's constant, *c* represents the speed of light, *e* is the charge of an electron, and λ is the incident light wavelength. All devices were stored in ambient atmosphere with no encapsulation during the device measurements.

Supporting Information

Supporting Information is available from the Wiley Online Library or from the author.

Acknowledgements

The work was supported by the National Natural Science Foundation of China (61974014) and the EPSRC Future Compound Semiconductor Manufacturing Hub (EP/P006973/1).

Conflict of Interest

The authors declare no conflict of interest.

Keywords

flexible devices, perovskites, photodetector arrays, self-powered devices

Received: January 1, 2020
Revised: March 25, 2020
Published online:

[1] Z. Bao, X. Chen, *Adv. Mater.* **2016**, *28*, 4177.
[2] K. Xu, Y. Lu, K. Takei, *Adv. Mater. Technol.* **2019**, *4*, 1800628.
[3] H. Xu, X. Han, X. Dai, W. Liu, J. Wu, J. Zhu, D. Kim, G. Zou, K. A. Sablon, A. Sergeev, Z. Guo, H. Liu, *Adv. Mater.* **2018**, *30*, 1706561.
[4] G. Konstantatos, I. Howard, A. Fischer, S. Hoogland, J. Clifford, E. Klem, L. Levina, E. H. Sargent, *Nature* **2006**, *442*, 180.
[5] X. Wang, Z. Cheng, K. Xu, H. K. Tsang, J.-B. Xu, *Nat. Photonics* **2013**, *7*, 888.
[6] Y. Q. Bie, Z. M. Liao, H. Z. Zhang, G. R. Li, Y. Ye, Y. B. Zhou, J. Xu, Z. X. Qin, L. Dai, D. P. Yu, *Adv. Mater.* **2011**, *23*, 649.

[7] M. Asif Khan, M. Shatalov, H. P. Maruska, H. M. Wang, E. Kuokstis, *Jpn. J. Appl. Phys.* **2005**, *44*, 7191.
[8] J. Michel, J. Liu, L. C. Kimerling, *Nat. Photonics* **2010**, *4*, 527.
[9] D. Guo, Q. Jiang, M. Tang, S. Chen, Y. I. Mazur, Y. Maidaniuk, M. Benamara, M. P. Semtsiv, W. T. Masselink, G. J. Salamo, H. Liu, J. Wu, *Semicond. Sci. Technol.* **2018**, *33*, 094009.
[10] A. Ren, L. Yuan, H. Xu, J. Wu, Z. Wang, *J. Mater. Chem. C* **2019**, *7*, 14441.
[11] T. Zhang, F. Wang, P. Zhang, Y. Wang, H. Chen, J. Li, J. Wu, L. Chen, Z. D. Chen, S. Li, *Nanoscale* **2019**, *11*, 2871.
[12] G. Azzellino, A. Grimoldi, M. Binda, M. Caironi, D. Natali, M. Sampietro, *Adv. Mater.* **2013**, *25*, 6829.
[13] P. Zhang, T. Zhang, Y. Wang, D. Liu, H. Xu, L. Chen, Y. Li, J. Wu, Z. D. Chen, S. Li, *J. Power Sources* **2019**, *439*, 227091.
[14] M. Li, M. Yu, S. Jiang, S. Liu, H. Liu, H. Xu, D. Su, G. Zhang, Y. Chen, J. Wu, *Mater. Horizons* **2020**, *6*, 130.
[15] A. Mei, X. Li, L. Liu, Z. Ku, T. Liu, Y. Rong, M. Xu, M. Hu, J. Chen, Y. Yang, M. Gratzel, H. Han, *Science* **2014**, *345*, 295.
[16] W. Nie, H. Tsai, R. Asadpour, A. J. Neukirch, G. Gupta, J. J. Crochet, M. Chhowalla, S. Tretiak, M. A. Alam, H. Wang, *Science* **2015**, *347*, 522.
[17] M. I. Saidaminov, V. Adinolfi, R. Comin, A. L. Abdelhady, W. Peng, I. Dursun, M. Yuan, S. Hoogland, E. H. Sargent, O. M. Bakr, *Nat. Commun.* **2015**, *6*, 8724.
[18] K. Shen, X. Li, H. Xu, M. Wang, X. Dai, J. Guo, T. Zhang, S. Li, G. Zou, K. Choy, I. P. Parkin, Z. Guo, H. Liu, J. Wu, *J. Mater. Chem. A* **2019**, *7*, 6134.
[19] Y. Wang, H. Xu, F. Wang, D. Liu, H. Chen, H. Zheng, L. Ji, P. Zhang, T. Zhang, Z. David Chen, J. Wu, L. Chen, S. Li, *Chem. Eng. J.* **2019**, 123589.
[20] D. Liu, Y. Wang, H. Xu, H. Zheng, T. Zhang, P. Zhang, F. Wang, J. Wu, Z. Wang, Z. Chen, S. Li, *Sol. RRL* **2019**, *3*, 1800292.
[21] Z. Shi, S. Li, Y. Li, H. Ji, X. Li, D. Wu, T. Xu, Y. Chen, Y. Tian, Y. Zhang, C. Shan, G. Du, *ACS Nano* **2018**, *12*, 1462.
[22] H. Wang, X. Zhang, Q. Wu, F. Cao, D. Yang, Y. Shang, Z. Ning, W. Zhang, W. Zheng, Y. Yan, S. V Kershaw, L. Zhang, A. L. Rogach, X. Yang, *Nat. Commun.* **2019**, *10*, 665.
[23] J. Song, J. Li, X. Li, L. Xu, Y. Dong, H. Zeng, *Adv. Mater.* **2015**, *27*, 7162.
[24] J. Li, L. Xu, T. Wang, J. Song, J. Chen, J. Xue, Y. Dong, B. Cai, Q. Shan, B. Han, H. Zeng, *Adv. Mater.* **2017**, *29*, 1603885.
[25] J. Tang, K. W. Kemp, S. Hoogland, K. S. Jeong, H. Liu, L. Levina, M. Furukawa, X. Wang, R. Debnath, D. Cha, K. W. Chou, A. Fischer, A. Amassian, J. B. Asbury, E. H. Sargent, *Nat. Mater.* **2011**, *10*, 765.
[26] A. Dong, X. Ye, J. Chen, Y. Kang, T. Gordon, J. M. Kikkawa, C. B. Murray, *J. Am. Chem. Soc.* **2011**, *133*, 998.
[27] C. Yi, J. Luo, S. Meloni, A. Boziki, N. Ashari-Astani, C. Grätzel, S. M. Zakeeruddin, U. Röthlisberger, M. Grätzel, *Energy Environ. Sci.* **2016**, *9*, 656.
[28] J. K. Nam, S. U. Chai, W. Cha, Y. J. Choi, W. Kim, M. S. Jung, J. Kwon, D. Kim, J. H. Park, *Nano Lett.* **2017**, *17*, 2028.
[29] M. Liu, G. Zhong, Y. Yin, J. Miao, K. Li, C. Wang, X. Xu, C. Shen, H. Meng, *Adv. Sci.* **2017**, *4*, 1700335.
[30] C. Liu, W. Li, H. Li, H. Wang, C. Zhang, Y. Yang, X. Gao, Q. Xue, H. Yip, J. Fan, R. E. I. Schropp, Y. Mai, *Adv. Energy Mater.* **2018**, *9*, 1803572.
[31] J.-N. Yang, Y. Song, J.-S. Yao, K.-H. Wang, J.-J. Wang, B.-S. Zhu, M.-M. Yao, S. U. Rahman, Y.-F. Lan, F.-J. Fan, H.-B. Yao, *J. Am. Chem. Soc.* **2020**, *142*, 2956.
[32] Q. D. Ling, S. Li, E. T. Kang, K. G. Neoh, B. Liu, W. Huang, *Surf. Interface Anal.* **2002**, *33*, 552.
[33] K. Yan, M. Long, T. Zhang, Z. Wei, H. Chen, S. Yang, J. Xu, *J. Am. Chem. Soc.* **2015**, *137*, 4460.
[34] L. Zhang, X. Yang, Q. Jiang, P. Wang, Z. Yin, X. Zhang, H. Tan, Y. Yang, M. Wei, B. R. Sutherland, E. H. Sargent, J. You, *Nat. Commun.* **2017**, *8*, 15640.
[35] D. J. Gundlach, T. N. Jackson, D. G. Schlom, S. F. Nelson, *Appl. Phys. Lett.* **1999**, *74*, 3302.
[36] S. Tsunekawa, T. Fukuda, A. Kasuya, *J. Appl. Phys.* **2000**, *87*, 1318.
[37] P. Zhao, W. Yin, M. Kim, M. Han, Y. J. Song, T. K. Ahn, H. S. Jung, *J. Mater. Chem. A* **2017**, *5*, 7905.
[38] H. Wang, D. H. Kim, *Chem. Soc. Rev.* **2017**, *46*, 5204.
[39] X. Li, Y. Wu, S. Zhang, B. Cai, Y. Gu, J. Song, H. Zeng, *Adv. Funct. Mater.* **2016**, *26*, 2435.
[40] Y. Wu, C. Wei, X. Li, Y. Li, S. Qiu, W. Shen, B. Cai, Z. Sun, D. Yang, Z. Deng, H. Zeng, *ACS Energy Lett.* **2018**, *3*, 2030.
[41] I. Lignos, S. Stavrakis, G. Nedelcu, L. Protesescu, A. J. Demello, M. V. Kovalenko, *Nano Lett.* **2016**, *16*, 1869.
[42] P. Liu, W. Chen, W. Wang, B. Xu, D. Wu, J. Hao, W. Cao, F. Fang, Y. Li, Y. Zeng, R. Pan, S. Chen, W. Cao, X. W. Sun, K. Wang, *Chem. Mater.* **2017**, *29*, 5168.
[43] J. Cao, S. X. Tao, P. A. Bobbert, C.-P. Wong, N. Zhao, *Adv. Mater.* **2018**, *30*, 1707350.
[44] M. Abdi-Jalebi, Z. Andaji-Garmaroudi, S. Cacovich, C. Stavrakas, B. Philippe, J. M. Richter, M. Alsari, E. P. Booker, E. M. Hutter, A. J. Pearson, S. Lilliu, T. J. Savenije, H. Rensmo, G. Divitini, C. Ducati, R. H. Friend, S. D. Stranks, *Nature* **2018**, *555*, 497.
[45] Z. Zhang, Y. Zhu, W. Wang, W. Zheng, R. Lin, F. Huang, *J. Mater. Chem. C* **2018**, *6*, 446.
[46] V. D. Mihailetchi, P. W. M. Blom, J. C. Hummelen, M. T. Rispens, *J. Appl. Phys.* **2003**, *94*, 6849.
[47] G. G. Malliaras, J. R. Salem, P. J. Brock, J. C. Scott, *J. Appl. Phys.* **1998**, *84*, 1583.
[48] Q. Chen, L. Mao, Y. Li, T. Kong, N. Wu, C. Ma, S. Bai, Y. Jin, D. Wu, W. Lu, B. Wang, L. Chen, *Nat. Commun.* **2015**, *6*, 7745.
[49] W. Ye, J. Xiang, F. Huang, D. Zhong, *Mater. Res. Express* **2018**, *5*, 085506.
[50] C. Li, C. Han, Y. Zhang, Z. Zang, M. Wang, X. Tang, J. Du, *Sol. Energy Mater. Sol. Cells* **2017**, *172*, 341.
[51] B. Yang, F. Zhang, J. Chen, S. Yang, X. Xia, T. Pullerits, W. Deng, K. Han, *Adv. Mater.* **2017**, *29*, 1703758.
[52] X. Li, D. Yu, J. Chen, Y. Wang, F. Cao, Y. Wei, Y. Wu, L. Wang, Y. Zhu, Z. Sun, J. Ji, Y. Shen, H. Sun, H. Zeng, *ACS Nano* **2017**, *11*, 2015.
[53] M. I. Saidaminov, M. A. Haque, J. Almutlaq, S. Sarmah, X.-H. Miao, R. Begum, A. A. Zhumekenov, I. Dursun, N. Cho, B. Murali, O. F. Mohammed, T. Wu, O. M. Bakr, *Adv. Opt. Mater.* **2017**, *5*, 1600704.
[54] J. Zhang, Q. Wang, X. Zhang, J. Jiang, Z. Gao, Z. Jin, S. Liu, *RSC Adv.* **2017**, *7*, 36722.
[55] F. Cao, L. Meng, M. Wang, W. Tian, L. Li, *Adv. Mater.* **2019**, *31*, 1806725.
[56] H. Deng, X. Yang, D. Dong, B. Li, D. Yang, S. Yuan, K. Qiao, Y.-B. Cheng, J. Tang, H. Song, *Nano Lett.* **2015**, *15*, 7963.
[57] W. Wu, X. Wang, X. Han, Z. Yang, G. Gao, Y. Zhang, J. Hu, Y. Tan, A. Pan, C. Pan, *Adv. Mater.* **2019**, *31*, 1805913.
[58] H. Sun, T. Lei, W. Tian, F. Cao, J. Xiong, L. Li, *Small* **2017**, *13*, 1701042.
[59] Y. Li, L. Meng, Y. Yang, G. Xu, Z. Hong, Q. Chen, J. You, G. Li, Y. Yang, Y. Li, *Nat. Commun.* **2016**, *7*, 10214.
[60] A. Dualeh, N. Tétreault, T. Moehl, P. Gao, M. K. Nazeeruddin, M. Grätzel, *Adv. Funct. Mater.* **2014**, *24*, 3250.